FRONTIERS OF PHYSICS

RESEARCH ARTICLE
Volume 19 / Issue 5 / 53205 / 2024

Optimizing hydrogen evolution reaction: Computational screening of single metal atom impurities in 2D MXene $Nb_4C_3O_2$

Željko Šljivančanin

Vinča Institute of Nuclear Sciences - National Institute of the Republic of Serbia, University of Belgrade, P.O. Box 522, RS-11001 Belgrade, Serbia
E-mail: zeljko@vin.bg.ac.rs
Received December 1, 2023; accepted February 20, 2024

ABSTRACT

MXenes, a novel class of 2D transition metal carbides and nitrides, have recently emerged as a promising candidate in the quest for efficient catalysts for the hydrogen evolution reaction. To enhance the performance of 2D MXenes with modest or poor catalytic efficiency, a particularly prosperous strategy involves doping with transition and noble metal atoms. Taking the $Nb_4C_3O_2$ monolayer as a model, we explore substitutional metallic impurities, which serve as single-atom catalysts embedded within the $Nb_4C_3O_2$ surface. Our findings demonstrate the ability to finely tune the atomic H binding energy within a 0.6 eV range, showing the potential for precise control in catalytic applications. Across different transition and noble metals, the single atoms integrated into $Nb_4C_3O_2$ effectively adjust the free energy of H adsorption at nearby O atoms, achieving values comparable to or superior to Pt catalysts. A comprehensive examination of the electronic properties around the impurities reveals a correlation between changes in local reactivity and charge transfer to neighboring O atoms, where H atoms bind.

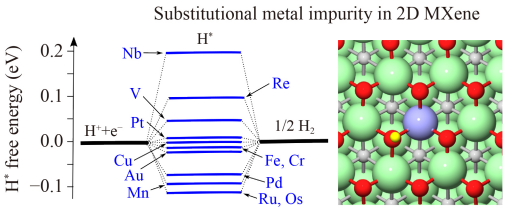

Keywords hydrogen evolution reaction, MXenes, DFT, single-atom catalysts

1 Introduction

Hydrogen has been recognized as a promising candidate for environmentally friendly energy storage, aiming to replace traditional fossil fuels and mitigate their undesirable consequences. Green hydrogen production, a vital component of this shift, relies on utilizing solar, wind, or hydropower to electrolytically split water into hydrogen and oxygen. The electrocatalysts used to efficiently produce hydrogen play a crucial role in the shift. Extensive experimental efforts to synthesize novel electrocatalysts with improved efficiency have been complemented by tremendous progress in computational modeling based on density functional theory (DFT). In addition to creating possibilities for the computer-aided design of new catalysts, the merging theory and experiment enables an understanding of the origin of the reactivity of the electrodes at the microscopic level [1, 2]. Nørskov and collaborators [3–5] have formulated a straightforward theory to quantify surface efficiency in catalyzing the hydrogen evolution reaction (HER). They identified the Gibbs free energy of hydrogen adsorption [ΔG(H)] as a pivotal descriptor for catalyst activity, emphasizing the importance of a value close to zero for optimal performance. State-of-the-art HER catalysts in acidic environments predominantly feature platinum. However, the scarcity and high cost of platinum have prompted extensive research into more cost-effective alternatives. This quest

Higher Education Press

https://doi.org/10.1007/s11467-024-1392-9

has led to a focus on a novel class of low-dimensional structures, including metal nanoparticles [6, 7], alloys [4], single-atom catalysts [18, 19], two-dimensional (2D) materials [8], and several types of heterostructures [9–11]. Complex nanostructures and interfaces with liquids were also investigated due to their relevance for green technologies other than environmentally friendly hydrogen production [12, 13]. Noteworthy among these 2D materials are MoS_2 nanoparticles supported by graphene oxide [14], metallic MoS_2 nanosheets [15], the edges of MoS_2 [16, 17], the MoS_2 doped with metal single atoms [18], and various MoS_2 nanocomposites [20], demonstrating promising catalytic properties.

MXenes, a recently discovered family of two-dimensional transition metal carbides, nitrides, or carbonitrides [21–24], have also emerged as promising candidates for the next generation of HER catalysts [25–31]. Doping MXenes with single transition or noble metals significantly enhances their catalytic properties, transforming them into single-atom catalysts embedded in 2D materials [32–34]. Examples include Pt single atoms in passivated Mo_2TiC_2 [35], Co single atom substitution in 2D molybdenum carbide [36], and Ru single atoms in nitrogen-doped Ti_3C_2 [37]. Moreover, nitrogen [38] and phosphorus doping [39] have been explored to further enhance the performance of MXenes. A recent DFT study focused on experimentally realized MXenes (T_2C, V_2C, Nb_2C, Ti_3C_2, and Nb_4C_3) terminated with oxygen, revealing high structural stability [26]. Among them, Ti_2CO_2 and Nb_2CO_2 displayed calculated ΔG(H) values very close to zero, indicating prospects for being effective nonprecious HER catalysts. However, V_2CO_2 and $Ti_3C_2O_2$ exhibited stronger than optimal hydrogen binding [26]. Notably, the $Nb_4C_3O_2$ showed weaker reactivity than required for good-performance HER catalysis, with DFT-calculated free energy of H adsorption in the range from 0.14 to 0.36 eV [26, 27], without an apparent reason for such a significant discrepancy. Yet, there are several advantageous properties of the $Nb_4C_3O_2$ granting it the status of the promising catalytic material. In addition to demonstrated structural stability, $Nb_4C_3O_2$ is a good conductor with a hydrophilic surface, which is advantageous in applications where the interaction with water is essential. The primary challenge lies in enhancing its reactivity to achieve close-to-optimal hydrogen binding.

The previous DFT studies of the HER on the $Nb_4C_3O_2$, as well as the investigations performed with other 2D MXenes in the pristine form or when doped with transition metals, were primarily focused on finding systems with favorable thermodynamics of the H binding. This study aims to go further and rationalize microscopic mechanisms driving the reactivity of the oxygen-terminated 2D Mixens doped with single-metal atom impurities. Using the $Nb_4C_3O_2$ as an example, we established a general picture of how to tune the H binding on a broad class of 2D materials featuring surface O atoms as the active catalytic sites. Through the utilization of DFT calculations, this paper demonstrates the potential of substituting $3d$, $4d$, and $5d$ transition and noble metals as impurities to transform the $Nb_4C_3O_2$ monolayer into a highly efficient catalyst for the HER. The electronic properties of the impurity atom play a crucial role in inducing changes in the local electronic structure of the 2D MXene, thereby significantly influencing hydrogen binding. In some instances, these changes lead to ΔG(H) values approaching zero, signifying enhanced efficiency in HER catalysis. A comprehensive exploration of the reactivity trends is conducted by comparing a diverse range of transition and noble metals considered as substitutional impurities in $Nb_4C_3O_2$. The observed trends in reactivity will be systematically rationalized based on the analysis of the electronic properties inherent in the studied MXenes.

The manuscript is structured into four sections. Following the Introduction, Section 2 details the computational methodology employed in this study. Section 3 presents the results along with their discussion, and the paper concludes with Section 4.

2 Computational methods

The DFT calculations were performed by GPAW code [40, 41], based on the projector augmented waves method (PAW) [42, 43]. We used atomic PAW setups where O-2s, 2p and Te-4s, 4p, 5s, 5p and 4d electrons were treated as valence electrons [44]. The wavefunctions were represented using the plane wave basis set with the energy cutoff of 600 eV. The $Nb_4C_3O_2$ monolayer was modeled using 3×3 surface cell, employing the periodic boundary conditions in the planes of the monolayer. The simulation cell included the vacuum of at least 16 Å in the direction perpendicular to the slab. The surface Brillouin zone was sampled by 16 special Monkhorst–Pack **k**-points [45], corresponding to the (4×4) grid centered on the Γ-point. The electronic exchange and correlation effects were described by employing the GGA-PBE functional [46]. The spin-polarization effects were included for magnetic $3d$ impurities. The iterative diagonalization of the Kohn–Sham Hamiltonian was carried out by applying the Davidson method [47]. To facilitate the convergency procedure, the electronic states were occupied according to the Fermi–Dirac distribution corresponding to the temperature of 0.05 eV. The geometry optimization was performed through the Broyden–Fletcher–Goldfarb–Shanno algorithm [48], as implemented in the Atomic Simulation Environment (ASE) python package [49, 51]. The ASE package is also used to set the atomic structure of studied systems and for postprocessing of data obtained from DFT calculations. The electron charges of the individual atoms were calculated by employing Bader approach [50]. The H

adsorption energy is calculated as

$$E_{\text{ads}}(\text{H}) = E(\text{H/Mxene}) - E(\text{Mxene}) - 1/2\,E(\text{H}_2), \quad (1)$$

where E(H/Mxene), E(Mxene), and $E(\text{H}_2)$ are total energies of the H atom adsorbed on the the surface of MXene, the total energy of the Mxene, and the energy of the H_2 molecule in the gas phase. The free energy of H adsorption $\Delta G(\text{H})$ is directly connected to the H adsorption energy $E_{\text{ads}}(\text{H})$ via the expression as follows:

$$\Delta G(\text{H}) = E_{\text{ads}}(\text{H}) + \Delta E_{\text{ZPE}} - T\Delta S_{\text{H}}. \quad (2)$$

The ΔE_{ZPE} and ΔS_{H} are differences in the zero-point energy and the entropy of the adsorbed H atom and the hydrogen in the gas phase. Following approach from Ref. [3] the $\Delta G(\text{H})$ and $E_{\text{ads}}(\text{H})$ are connected by a simple formula: $\Delta G(\text{H}) = E_{\text{ads}}(\text{H}) + 0.24$ eV.

The binding energies of the metal impurity M in the MXene with an Nb vacancy are calculated according to the standard expression:

$$E_{\text{B}}(\text{M}) = E(\text{M}) + E(\text{vac} - \text{Nb}_4\text{C}_3\text{O}_2) - E(\text{M} - \text{Nb}_4\text{C}_3\text{O}_2), \quad (3)$$

where the terms in the formula above are the total energies of free atom M, the Mxene with the Nb vacancy, and the $\text{Nb}_4\text{C}_3\text{O}_2$ with an Nb surface atom substituted by metal M.

3 Results and discussion

3.1 Substitutional metal impurities

To assess the stability of the doped $\text{Nb}_4\text{C}_3\text{O}_2$ monolayer, we first calculated the binding of metal atom $E_B(M)$ at the Nb vacancies created on the surface of the $\text{Nb}_4\text{C}_3\text{O}_2$ monolayer (Fig. 1), using as the reference energies those of free metal atoms. The calculated energies are listed in Table 1.

The set of inspected impurities expands over $3d$, $4d$, and $5d$ elements from Groups IV–XII. The $4d$ element Tc is not included in the study as a radioactive element unsuitable for green hydrogen production. The binding energy of Nb in Table 1 is the energy cost of removing an Nb atom from the surface layer to the gas phase. As expected, the calculated binding energies show a clear trend of a monotonic decrease when moving from early to late transition and noble metals. Also, the binding is weaker for $3d$ than $4d$ metals and reaches the highest values for $5d$ elements. The exceptions are Groups XI and XII elements, where displacements of impurities from the plane formed by Nb atoms could be larger than 2 Å, and the metal adsorption geometries differ considerably. Furthermore, these metals bind significantly weaker than others; thus, the structures they form are less stable than those of other metal impurities.

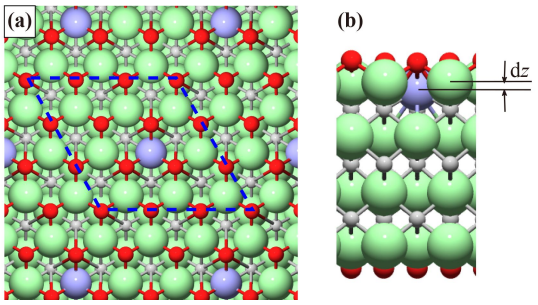

Fig. 1 Top **(a)** and side **(b)** view of the atomic structure of substitutional metal impurity in $\text{Nb}_4\text{C}_3\text{O}_2$. The impurity atoms are depicted as blue spheres. Nb, C, and O atoms are presented as green, light gray, and red spheres. The dz in panel (b) marks impurity displacement out of the surface Nb plane.

3.2 Hydrogen adsorption

Our tests and previous studies [52] show that the H atoms at $\text{Nb}_4\text{C}_3\text{O}_2$ prefer binding on oxygens. We also found that the impurity effect on the H binding is well-localized to the O atoms next to the impurity, and hence, all numbers in Table 2 correspond to these adsorption sites. An example of the H adsorption geometry is depicted in Fig. 2.

We calculated the free adsorption energy of the H atom at pristine $\text{Nb}_4\text{C}_3\text{O}_2$ monolayer of 0.20 eV

Table 1 Binding energies (E_{B}) of substitutional metal impurities in $\text{Nb}_4\text{C}_3\text{O}_2$ monolayer and their displacements (dz) from the surface Nb atomic plane.

Group	Impurity	E_{B} (eV)	dz (Å)	Impurity	E_{B} (eV)	dz (Å)	Impurity	E_{B} (eV)	dz (Å)
IV	Ti	9.60	0.11	Zr	11.02	0.31	Hf	11.73	0.27
V	V	7.92	–0.19	Nb	10.11	0.00	Ta	11.77	0.08
VI	Cr	5.34	–0.06	Mo	7.80	–0.20	W	9.90	–0.18
VII	Mn	4.51	–0.07	Tc	–	–	Re	8.15	–0.28
VIII	Fe	4.98	–0.37	Ru	6.40	–0.31	Os	7.52	–0.33
IX	Co	5.80	–0.68	Rh	5.66	–0.53	Ir	5.79	–0.29
X	Ni	5.05	–0.66	Pd	2.83	–0.44	Pt	4.05	–0.56
XI	Cu	3.09	–0.46	Ag	1.60	2.06	Au	0.35	–0.29
XII	Zn	1.56	1.31	Cd	0.47	1.80	Hg	unstable	–

Table 2 Free energy of H adsorption (ΔG) and the effective charge transfer on an O atom in the vicinity of the impurity (ΔQ) at $Nb_4C_3O_2$ monolayer with substitutional metal impurities.

Group	Impurity	ΔG (eV)	ΔQ (e)	Impurity	ΔG (eV)	ΔQ (e)	Impurity	ΔG (eV)	ΔQ (e)
IV	Ti	0.14	–0.003	Zr	0.36	0.038	Hf	0.36	0.045
V	V	0.05	–0.030	Nb	0.20	0.000	Ta	0.32	0.016
VI	Cr	–0.01	–0.046	Mo	0.14	–0.034	W	0.17	–0.015
VII	Mn	–0.09	–0.055	Tc	–	–	Re	0.10	–0.041
VIII	Fe	–0.01	–0.089	Ru	–0.11	–0.088	Os	–0.11	–0.062
IX	Co	–0.15	–0.106	Rh	–0.19	–0.125	Ir	–0.17	–0.088
X	Ni	–0.18	–0.107	Pd	–0.07	–0.129	Pt	0.01	–0.136
XI	Cu	0.00	–0.111	Ag	0.13	–0.058	Au	–0.02	–0.139
XII	Zn	0.28	0.014	Cd	0.30	–0.011	Hg	–	–

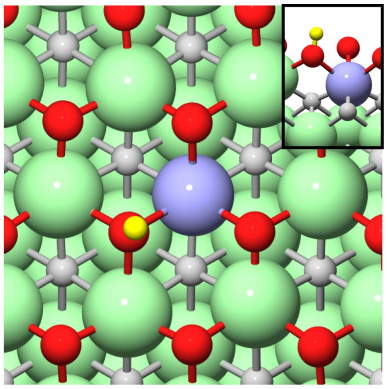

Fig. 2 The top view of the H adsorption geometry at $Nb_4C_3O_2$ monolayer with Mn impurity. The side view is shown in the inset. Blue and yellow spheres represent Mn and H atoms. The color coding of other atoms is the same as in Fig. 1.

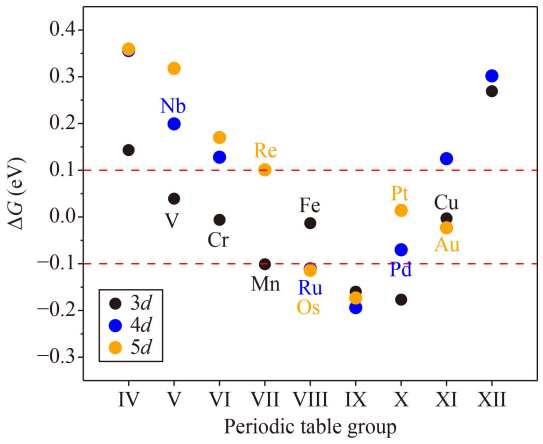

Fig. 3 The variation in ΔG(H) with the Group number of substitutional impurity in $Nb_4C_3O_2$ monolayer. The points corresponding to Nb (representing the pristine $Nb_4C_3O_2$) and impurities giving rise to the $|\Delta G(\mathrm{H})| \leq 0.1$ eV are labeled.

(Table 2), not far from the value in Ref. [26]. Since this MXene is not among those with the optimal catalytic properties regarding the HER, further modifications are required to improve its efficiency. A convenient and efficient approach to tailor $Nb_4C_3O_2$ reactivity relies on doping with transition and noble metal atoms. Our systematic study of 3*d*, 4*d*, and 5*d* transition and noble metals incorporated into $Nb_4C_3O_2$ demonstrates that these single-atom impurities can be used for an effective adjustment of the free energy of H adsorption at nearby O atoms over the energy range of ~0.6 eV (Fig. 3). The plot in Fig. 3 shows an increase in the reactivity of the O adsorption sites with an increase in the occupation of the impurity *d* shell. Once it gets fully occupied, the binding of H weakens. The highest H binding (the lowest ΔG(H) values) occurs for the Group IX or X impurites. In Fig. 3 we highlighted the impurities that produce ΔG(H) values in the range from –0.1 to 0.1 eV, and hence convert the $Nb_4C_3O_2$ monolayer into a highly efficient catalyst for HER. The list of the impurities includes 3*d* metals V, Cr, Fe, Mn, Fe, and Cu, Pd as a 4*d* metal, as well as 5*d* elements Re, Pt, and Au. The Ru, and Os are marginally (by 0.01 eV) outside this energy window and should also be considered promising candidates to tune the $Nb_4C_3O_2$ reactivity in the desired direction.

To rationalize the impurity effect on the H binding and trends across the periodic table, in Fig. 4, we plotted ΔG(H) dependence on the center of the 2*p* states of O adsorption site prior to H binding. The plot is inspired by the well-known *d*-band model of Hammer and Nørskov [53] successfully used to quantify the reactivity of metal surfaces. The correlation between the position of O-2*p* center and the ΔG(H) is apparent for 3*d* metal impurities and less evident for 4*d* and 5*d* elements. We attribute the dispersion of the point in the plot from a straight line, which would correspond to the perfect correlation, to the difference in the adsorption geometries of metal impurities embedded into the $Nb_4C_3O_2$. As seen in Table 1, the d*z* meassuring displacement of single-atom impurities from the Nb atomic plane varies from –0.68 to 2.06 Å. Thus, the intrinsic assumptions of the theories like the *d*-band model that we compare only very similar adsorption geometries is fulfilled only aproximately. Still, the plot reveals that the major trend in

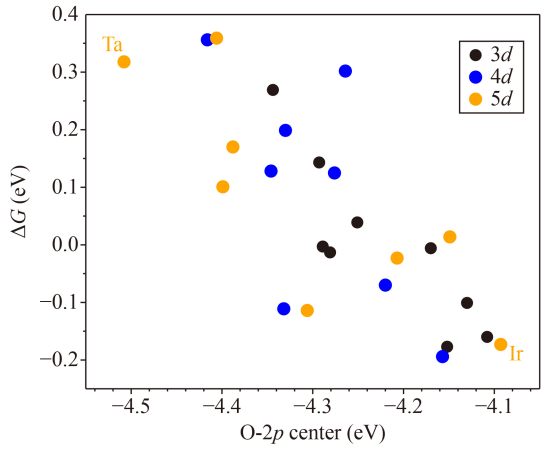

Fig. 4 The correlation between ΔG(H) and the 2p center of the O atoms where H binds, for $Nb_4C_3O_2$ monolayer with 3d, 4d and 5d transition and noble metal impurities.

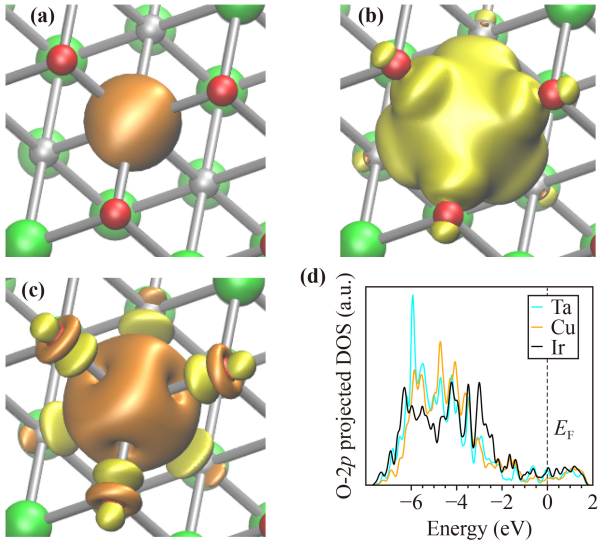

Fig. 5 Impurity-induced charge density perturbation $\delta\rho$ in $Nb_4C_3O_2$ monolayer with **(a)** Ta, **(b)** Cu, and **(c)** Ir substitutional impurities; $\delta\rho$ is defined as the difference in the charge densities of the MXene with the impurity and the pristine one; the orange and yellow isocontours are plotted at the values of 0.05 e/Å^3 and –0.05 e/Å^3, respectively. **(d)** DOS projected on the 2p states of an O atom next to the impurity. The color scheme: Nb – green; O – red; C – gray. The impurities atoms are enclosed in orange and yellow isocontoures and thus not visible.

reactivity can be understtod as the electronic effect. In Fig. 4, we highlighted as examples Ta and Ir the impurities with the lowest ΔG(H) and the highest O-2p center positions. At the 2D MXene with Ta impurity, the ΔG(H) is 0.32 eV, and the corresponding value for Ir is –0.17 eV. It is evident that the upshift of O-2p center by ~0.4 eV leads to an increase of H binding by 0.49 eV. For pristine $Nb_4C_3O_2$ monolayer, we calculated ΔG(H) of 0.20 eV. The correlation between the O-2p center and the ΔG(H) raises the question of the origin of the changes in the position of the O-2p center. To get insight into this issue, we further compared $Nb_4C_3O_2$ monolayer with Ta and Ir, focusing on the impurity atoms and three O atoms nearby. In addition to Ta, and Ir, in further analysis of the electronic properties of doped $Nb_4C_3O_2$ we also included Cu, the metal with theoretically optimal ΔG(H) value of zero. For these three transition metals, in Figs. 5(a)–(c), we plotted the impurity-induced charge density $\delta\rho$, defined as the difference in the charge densities of the $Nb_4C_3O_2$ with the impurity and the pristine monolayer. The isocontour plot of $\delta\rho$ for the $Nb_4C_3O_2$ monolayer with a Ta impurity [Fig. 5(a)] illustrates that alterations in electron density induced by Ta are concentrated around the impurity, with minimal and invisible effects on the three closest O atoms, as depicted in the figure. This observation aligns seamlessly with small differences in ΔG(H) observed between the pristine and Ta-doped $Nb_4C_3O_2$ monolayer. A distinctive contrast emerges in the $\delta\rho$ plot when examining Cu or Ir impurities in $Nb_4C_3O_2$ [Figs. 5(b) and (c)]. Beyond the electron density perturbation at the impurity site, noticeable changes manifest at the neighboring O atoms. This is exemplified by an apparent depletion of the O-2p orbital oriented toward the impurity atom. The electron depletion on the O atoms signifies the elevated electronegativity of Cu or Ir relative to Nb. Figure 5(d) illustrates the impact of three different impurities on the energy of the 2p states of the adjacent O atoms. The evident energy shift of the O states in the MXene with an Ir impurity, compared to that doped with a Ta atom, contributes to higher reactivity of the former, resulting in significantly stronger H binding. Notably, the Cu impurity induces changes in local electronic properties, representing a perfect compromise between Ta and Ir and hence providing an environment for optimal H binding. The $\delta\rho$ and density of states (DOS) projected onto nearby O-2p orbitals, as examined for other metals considered in this study, are consistent with the calculated ΔG(H) values. To quantify the effective charge transfer on O atoms near the metal impurity, the ΔQ, we employed the Bader analysis [50]. The values presented in Table 2 are calculated as the difference in the Bader charges of the O atom on the $Nb_4C_3O_2$ monolayer with the impurity compared to the value found for pristine $Nb_4C_3O_2$. The Bader analysis confirms that the free energies of the H adsorption can be correlated to the effective charge transfer on O atoms near the metal impurity.

4 Conclusions

Based on extensive DFT studies investigating metal impurities within $Nb_4C_3O_2$, our findings highlight several transition and noble metals capable of finely tuning the free energy of H adsorption. These tunable

values match or surpass those observed on the Pt(111) surface. Consequently, we identify the corresponding 2D structures as highly promising candidates for efficiently catalyzing the hydrogen evolution reaction. The list of the single-atom metals eble to tune H binding on the $Nb_4C_3O_2$ monolayer to theoretically optimal value includes cheap and widely available elements Fe, Cr, and Cu. Our study reveals that enhanced hydrogen binding occurs in the presence of impurities exhibiting higher electronegativity than Nb. This effect stems from the effective electron depletion these impurities induce in the oxygen sites where hydrogen binds. We anticipate that this alteration in local reactivity, driven by oxygen charging, is a general phenomenon extending beyond $Nb_4C_3O_2$ to other 2D MXenes. This broadens the scope of our findings, suggesting the broader applicability of substitutional impurities for tuning reactivity in diverse 2D materials.

Acknowledgements This work has been supported by the Serbian Academy of Sciences and Arts under Grant No. F-18. We thank the Advanced Scientific Computing Center of the Texas A&M University at Qatar for providing us access to the RAAD supercomputer.

References and notes

1. Y. Zheng, Y. Jiao, M. Jaroniec, and S. Z. Qiao, Advancing the electrochemistry of the hydrogen-evolution reaction through combining experiment and theory, *Angew. Chem. Int. Ed.* 54(1), 52 (2015)
2. M. Luo, J. T. Yang, X. G. Li, M. Eguchi, Y. Yamauchi, and Z. L. Wang, Insights into alloy/oxide or hydroxide interfaces in Ni–Mo-based electrocatalysts for hydrogen evolution under alkaline conditions, *Chem. Sci. (Camb.)* 14(13), 3400 (2023)
3. J. K. Nørskov, T. Bligaard, T. A. Logadottir, J. R. Kitchin, J. G. Chen, S. Pandelov, and U. Stimming, Trends in the exchange current for hydrogen evolution, *J. Electrochem. Soc.* 152(3), J23 (2005)
4. J. Greeley, T. F. Jaramillo, J. Bonde, I. B. Chorkendorff, and J. K. Nørskov, Computational high-throughput screening of electrocatalytic materials for hydrogen evolution, *Nat. Mater.* 5(11), 909 (2006)
5. J. K. Nørskov, T. Bligaard, J. Rossmeisl, and C. H. Christensen, Towards the computational design of solid catalysts, *Nat. Chem.* 1(1), 37 (2009)
6. J. Mahmood, F. Li, S. M. Jung, M. S. Okyay, I. Ahmad, S. J. Kim, N. Park, H. Y. Jeong, and J. B. Baek, An efficient and pH-universal ruthenium-based catalyst for the hydrogen evolution reaction, *Nat. Nanotechnol.* 12(5), 441 (2017)
7. Z. X. Zhu, Y. X. Lin, P. Fang, M. S. Wang, M. Z. Zhu, X. Y. Zhang, J. S. Liu, J. G. Hu, and X. Y. Xu, Orderly nanodendritic nickel substitute for Raney nickel catalyst improving alkali water electrolyzer, *Adv. Mater.* 36(1), 2307035 (2024)
8. H. Y. Jin, C. X. Guo, X. Liu, J. L. Liu, A. Vasileff, Y. Jiao, Y. Zheng, and S. Z. Qiao, Emerging two-dimensional nanomaterials for electrocatalysis, *Chem. Rev.* 118(13), 6337 (2018)
9. M. Gong, W. Zhou, M. C. Tsai, J. G. Zhou, M. Y. Guan, M. C. Lin, B. Zhang, Y. F. Hu, D. Y. Wang, J. Yang, S. J. Pennycook, B. J. Hwang, and H. J. Dai, Nanoscale nickel oxide/nickel heterostructures for active hydrogen evolution electrocatalysis, *Nat. Commun.* 5(1), 4695 (2014)
10. L. Q. Wang, Y. X. Hao, L. M. Deng, F. Hu, S. Zhao, L. L. Li, and S. J. Peng, Rapid complete reconfiguration induced actual active species for industrial hydrogen evolution reaction, *Nat. Commun.* 13(1), 5785 (2022)
11. P. Fang, M. Z. Zhu, J. Liu, Z. X. Zhu, J. G. Hu, and X. Y. Xu, Making ternary-metal hydroxy-sulfide catalyst via cathodic reconstruction with ion regulation for industrial-level hydrogen generation, *Adv. Energy Mater.* 13(35), 2301222 (2023)
12. L. Bian, Z. Y. Zhang, H. Tian, N. N. Tian, Z. Ma, and Z. L. Wang, Grain boundary-abundant copper nanoribbons on balanced gas–liquid diffusion electrodes for efficient CO_2 electroreduction to C_2H_4, *Chin. J. Catal.* 54, 199 (2023)
13. Z. Y. Zhang, H. Tian, L. Bian, S. Z. Liu, Y. Liu, and Z. L. Wang, Cu–Zn-based alloy/oxide interfaces for enhanced electroreduction of CO_2 to C_{2+} products, *J. Energy Chem.* 83, 90 (2023)
14. Y. G. Li, H. L. Wang, L. M. Xie, Y. Y. Liang, G. S. Hong, and H. J. Dai, MoS_2 nanoparticles grown on graphene: An advanced catalyst for the hydrogen evolution reaction, *J. Am. Chem. Soc.* 133(19), 7296 (2011)
15. M. A. Lukowski, A. S. Daniel, F. Meng, A. Forticaux, L. S. Li, and S. Jin, Enhanced hydrogen evolution catalysis from chemically exfoliated metallic MoS_2 nanosheets, *J. Am. Chem. Soc.* 135(28), 10274 (2013)
16. B. Hinnemann, P. G. Moses, J. Bonde, K. P. Jørgensen, J. H. Nielsen, S. Horch, I. B. Chork-endorff, and J. K. Nørskov, Biomimetic hydrogen evolution: MoS_2 nanoparticles as catalyst for hydrogen evolution, *J. Am. Chem. Soc.* 127(15), 5308 (2005)
17. C. Tsai, F. Abild-Pedersen, and J. K. Nørskov, Tuning the MoS_2 edge-site activity for hydrogen evolution via support interactions, *Nano Lett.* 14(3), 1381 (2014)
18. J. Deng, H. Li, J. Xiao, Y. Tu, D. Deng, H. Yang, H. Tian, J. Li, P. Ren, and X. Bao, Triggering the electrocatalytic hydrogen evolution activity of the inert two-dimensional MoS_2 surface via single-atom metal doping, *Energy Environ. Sci.* 8(5), 1594 (2015)
19. V. Ramalingam, P. Varadhan, H. C. Fu, H. Kim, D. L. Zhang, S. M. Chen, L. Song, D. Ma, Y. Wang, H. N. Alshareef, and J. H. He, Heteroatom-mediated interactions between ruthenium single atoms and an MXene support for efficient hydrogen evolution, *Adv. Mater.* 31(48), 1903841 (2019)
20. Q. Lu, Y. Yu, Q. Ma, K. Chen, and H. Zhang, 2D transition-metal-dichalcogenide-nanosheet-based composites for photocatalytic and electrocatalytic hydrogen evolution reactions, *Adv. Mater.* 28(10), 1917 (2016)
21. M. Naguib, O. Mashtalir, C. Carle, V. Presser, J. Lu, L. Hultman, Y. Gogotsi, and M. W. Barsoum, Two-dimensional transition metal carbides, *ACS Nano* 6(2), 1322 (2012)

22. M. Khazaei, M. Arai, T. Sasaki, C. Y. Chung, N. S. Venkataramanan, M. Estili, Y. Sakka, and Y. Kawazoe, Novel electronic and magnetic properties of two-dimensional transition metal carbides and nitrides, *Adv. Funct. Mater.* 23(17), 2185 (2013)
23. B. Anasori, M. R. Lukatskaya, and Y. Gogotsi, 2D metal carbides and nitrides (MXenes) for energy storage, *Nat. Rev. Mater.* 2(2), 16098 (2017)
24. X. T. Jiang, A. V. Kuklin, A. Baev, Y. Q. Ge, H. Ågren, H. Zhang, and P. N. Prasad, Two-dimensional MXenes: From morphological to optical, electric, and magnetic properties and applications, *Phys. Rep.* 848, 1 (2020)
25. Z. W. Seh, K. D. Fredrickson, B. Anasori, J. Kibsgaard, A. L. Strickler, M. R. Lukatskaya, Y. Gogotsi, T. F. Jaramillo, and A. Vojvodic, Two-dimensional molybdenum carbide (MXene) as an efficient electrocatalyst for hydrogen evolution, *ACS Energy Lett.* 1(3), 589 (2016)
26. G. Gao, A. P. O'Mullane, and A. Du, 2D MXenes: A new family of promising catalysts for the hydrogen evolution reaction, *ACS Catal.* 7(1), 494 (2017)
27. M. Pandey and K. S. Thygesen, Two-dimensional MXenes as catalysts for electrochemical hydrogen evolution: A computational screening study, *J. Phys. Chem. C* 121(25), 13593 (2017)
28. S. Bai, M. Yang, J. Jiang, X. He, J. Zou, Z. Xiong, G. Liao, and S. Liu, Recent advances of MXenes as electrocatalysts for hydrogen evolution reaction, *npj 2D Mater. Appl.* 5, 78 (2021)
29. Q. Kong, X. An, L. Huang, X. Wang, W. Feng, S. Qiu, Q. Wang, and C. Sun, A DFT study of $Ti_3C_2O_2$ MXenes quantum dots supported on single layer graphene: Electronic structure a hydrogen evolution performance, *Front. Phys.* 16(5), 53506 (2021)
30. Y. Tang, C. H. Yang, X. T. Xu, Y. Q. Kang, Y. Henzie, W. X. Que, and Y. Yamauchi, MXene nanoarchitectonics: Defect-engineered 2D MXenes towards enhanced electrochemical water splitting, *Adv. Energy Mater.* 12(12), 2103867 (2022)
31. T. Y. Shuai, Q. N. Zhan, H. M. Xu, Z. J. Zhang, and G. R. Li, Recent developments of MXene-based catalysts for hydrogen production by water splitting, *Green Chem.* 25(5), 1749 (2023)
32. N. C. Cheng, S. Stambula, D. Wang, M. N. Banis, J. Liu, A. Riese, B. W. Xiao, R. Y. Li, T. K. Sham, L. M. Liu, G. A. Botton, and X. L. Sun, Platinum single-atom and cluster catalysis of the hydrogen evolution reaction, *Nat. Commun.* 7(1), 13638 (2016)
33. A. Alarawi, V. Ramalingam, and J. H. He, Recent advances in emerging single atom confined two-dimensional materials for water splitting applications, *Mater. Today Energy* 11, 1 (2019)
34. D. N. Sredojević, M. R. Belić, and Ž. Šljivančanin, Hydrogen evolution reaction over single-atom catalysts based on metal adatoms at defected graphene and h-BN, *J. Phys. Chem. C* 124(31), 16860 (2020)
35. J. Zhang, Y. Zhao, X. Guo, C. Chen, C. L. Dong, R. S. Liu, C. P. Han, Y. Li, Y. Gogotsi, and G. Wang, Single platinum atoms immobilized on an MXene as an efficient catalyst for the hydrogen evolution reaction, *Nat. Catal.* 1(12), 985 (2018)
36. D. A. Kuznetsov, Z. Chen, P. V. Kumar, A. Tsoukalou, A. Kierzkowska, P. M. Abdala, O. V. Safonova, A. Fedorov, and C. R. Müller, Single site cobalt substitution in 2D molybdenum carbide (MXene) enhances catalytic activity in the hydrogen evolution reaction, *J. Am. Chem. Soc.* 141(44), 17809 (2019)
37. H. Liu, Z. Hu, Q. Liu, P. Sun, Y. Wang, S. Chou, Z. Hu, and Z. Zhang, Single-atom Ru anchored in nitrogen-doped MXene ($Ti_3C_2T_x$) as an efficient catalyst for the hydrogen evolution reaction at all pH values, *J. Mater. Chem. A* 8(46), 24710 (2020)
38. T. A. Le, Q. V. Bui, N. Q. Tran, Y. Cho, Y. Hong, Y. Kawazoe, and H. Lee, Synergistic effects of nitrogen doping on MXene for enhancement of hydrogen evolution reaction, *ACS Sustain. Chem. & Eng.* 7(19), 16879 (2019)
39. G. X. Qu, Y. Zhou, T. L. Wu, G. L. Zhao, F. F. Li, Y. J. Kang, and C. Xu, Phosphorized MXene-phase molybdenum carbide as an earth-abundant hydrogen evolution electrocatalyst, *ACS Appl. Energy Mater.* 1(12), 7206 (2018)
40. J. J. Mortensen, L. B. Hansen, and K. W. Jacobsen, Real-space grid implementation of the projector augmented wave method, *Phys. Rev. B* 71(3), 035109 (2005)
41. J. Enkovaara, C. Rostgaard, J. J. Mortensen, J. Chen, M. Dulak, L. Ferrighi, J. Gavnholt, C. Glinsvad, V. Haikola, H. A. Hansen, H. H. Kristoffersen, M. Kuisma, A. H. Larsen, L. Lehtovaara, M. Ljungberg, O. Lopez-Acevedo, P. G. Moses, J. Ojanen, T. Olsen, V. Petzold, N. A. Romero, J. Stausholm-Moller, M. Strange, G. A. Tritsaris, M. Vanin, M. Walter, B. Hammer, H. Hakkinen, G. K. H. Madsen, R. M. Nieminen, J. K. Norskov, M. Puska, T. T. Rantala, J. Schiotz, K. S. Thygesen, and K. W. Jacobsen, Electronic structure calculations with GPAW: A real-space implementation of the projector augmented-wave method, *J. Phys.: Condens. Matter* 22(25), 253202 (2010)
42. P. E. Blöchl, Projector augmented-wave method, *Phys. Rev. B* 50(24), 17953 (1994)
43. J. J. Mortensen, L. B. Hansen, and K. W. Jacobsen, Real-space grid implementation of the projector augmented wave method, *Phys. Rev. B* 71(3), 035109 (2005)
44. Homepage: wiki.fysik.dtu.dk/gpaw/setups/setups.html
45. H. J. Monkhorst and J. D. Pack, Special points for Brillouin-zone integrations, *Phys. Rev. B* 13(12), 5188 (1976)
46. J. P. Perdew, K. Burke, and M. Ernzerhof, Generalized gradient approximation made simple, *Phys. Rev. Lett.* 77(18), 3865 (1996)
47. E. R. Davidson, The iterative calculation of a few of the lowest eigenvalues and corresponding eigenvectors of large real-symmetric matrices, *J. Comput. Phys.* 17(1), 87 (1975)
48. D. C. Liu and J. Nocedal, On the limited memory BFGS method for large scale optimization, *Math. Program.* 45(1–3), 503 (1989)
49. S. R. Bahn and K. W. Jacobsen, An object-oriented scripting interface to a legacy electronic structure code, *Comput. Sci. Eng.* 4(3), 56 (2002)
50. R. F. W. Bader, Atoms in Molecules: A Quantum

Theory, New York: Oxford University Press, 1990

51. A. Hjorth Larsen, J. Jørgen Mortensen, J. Blomqvist, I. E. Castelli, R. Christensen, M. Dułak, J. Friis, M. N. Groves, B. Hammer, C. Hargus, E. D. Hermes, P. C. Jennings, P. Bjerre Jensen, J. Kermode, J. R. Kitchin, E. Leonhard Kolsbjerg, J. Kubal, K. Kaasbjerg, S. Lysgaard, J. Bergmann Maronsson, T. Maxson, T. Olsen, L. Pastewka, A. Peterson, C. Rostgaard, J. Schiøtz, O. Schütt, M. Strange, K. S. Thygesen, T. Vegge, L. Vilhelmsen, M. Walter, Z. Zeng, and K. W. Jacobsen, The atomic simulation environment — a Python library for working with atoms, *J. Phys.: Condens. Matter* 29(27), 273002 (2017)
52. Y. W. Cheng, J. H. Dai, J. M. Zhang, and Y. Song, Two-dimensional, ordered, double transition metal carbides (MXenes): A new family of promising catalysts for the hydrogen evolution reaction, *J. Phys. Chem. C* 122(49), 28113 (2018)
53. B. Hammer and J. K. Nørskov, Theoretical surface science and catalysis – Calculations and concepts, *Adv. Catal.* 45, 71 (2000)